



DEPARTMENT OF ENGINEERING CYBERNETICS

TTK4550 - SPECIALIZATION PROJECT

Design and Control of a Spring-actuated Jumping Quadruped in Earth Gravity

Author:

Johannes Ihle
Daniel Rosmæl Skauge

Supervisor:

Prof. Dr. Kostas Alexis

Co-supervisor:

Jørgen Anker Olsen

Date

Abstract

This specialization project involves the development of a concept design for a small, lightweight, and low-cost jumping quadruped robot, which jumps by releasing the energy stored in torsional springs embedded in parallel to the robots knee motor. The purpose of the robot is to be capable of jumping long distances in earth gravity, and to be used as a platform for testing quadruped jumping control algorithms. This goal must be seen in the context of the potential utility of jumping quadrupeds in extraterrestrial exploration, where they could traverse obstacles that would be insurmountable to wheeled rovers. The robot is designed to be small and lightweight to reduce the risk of damage during testing, and low-cost to make it more accessible to researchers. In addition to the general concept design, this report presents a Simulink Simscape simulation of the robot, used to evaluate various design choices. The report also presents a detailed CAD model for the spring-actuated leg, as well as an experiment-based system identification of the gear-friction of the selected motors. Using the identified friction characteristics of the motor, our simulations indicate a potential center of mass jump height of 0.5m for a robot with a total leg length of 20cm. TODO add the precise newest number.

Table of Contents

List of Figures	iv
List of Tables	v
1 Introduction	1
1.1 Motivation	1
1.2 Scope	1
1.3 Related Work	2
2 Theory	3
2.1 Actuator Modeling	3
2.1.1 DC Motor Model	3
2.1.2 BLDC Motor Model	3
2.1.3 Gear Transmission Friction Model	3
2.2 Spring Modeling	4
2.3 Kinematics, Jacobians, and Virtual Work	4
2.3.1 Robot Kinematics	4
2.3.2 Jacobian Matrix	5
2.3.3 Force/Torque Mapping	5
2.4 Contact Friction	6
2.5 Numerical Solvers	6
2.6 Linear Least Squares Regression	6
2.7 Inverse Kinematics	7
3 Modeling and Simulation	7
3.1 Simscape	7
3.2 Rigid Body Components of the Robot Model	9
3.3 Rigid Body Masses and Inertias	9
3.4 Elastic Components: Springs	11
3.5 Motor Modeling	13
3.6 Solver selection	13
4 Robot Design	13
4.1 The Single Vertical Manipulator Jump Model	13
4.2 Actuation Method Selection: Motors Only	14
4.3 Actuation Method Selection: Motors and Torsional Spring	16

4.4	Actuation Method Selection: Motors and Extension Spring	16
4.5	Hip Motor Strength Requirements	16
5	Motor Friction Estimation	17
5.1	Pendulum Modeling	17
5.2	Linear Regression Derivation	17
6	Link Length Optimization	18
6.1	Problem definition	19
6.2	Problem simplification	19
6.3	Initial Pose Calculation	19
6.4	Grid Search	21
7	Robot Hardware	21
7.1	Torsional Spring Leg	21
7.2	Extension Spring Leg design	22
7.3	Motor Selection	23
8	Results	24
8.1	Motor Friction Estimation	24
8.2	Link Length Optimization	24
8.3	Hip Motor Dimensioning Test	25
8.4	Motor Only Jumping Results	27
9	Discussion	28
9.1	Link Length Optimization Trade-offs	28
9.2	Limitations of the Symmetric Jump Model	28
9.3	Control and Dynamic Challenges	28
9.4	Design Considerations for Landing	29
10	Conclusion	29
10.1	Future work	29
11	Conclusion	29
Bibliography		30
Appendix		31
A	A06CLS V2 Website Information	31

B	A20BHM Website Information	31
C	A35CHM Motor Information	32
D	A80BHP-H Motor Information	32

List of Figures

1	Torque-speed characteristics of a BLDC motor. TODO: Replace with an image that isn't stolen, and that we are allowed to use.	3
2	Illustration of a 3 link robotic link arm in \mathbb{R}^2 with n links.	5
3	A typical Simscape block diagram.	8
4	A visualization of the model in figure 3.	8
5	Naming conventions for the parts of the robot, as well as forwards direction definition. TODO: name spines	9
6	Angle conventions for the robot body.	10
7	A figure displaying the conceptual difference between a parallel spring (right), as used in this work, and a series elastic spring (left) as used in the ANYmal robot [5].	12
8	A figure displaying the concept of a parallel extension spring, note that the spring generates torque directly in parallel with the knee joint just like for the parallel torsional spring seen in figure 7. Mathematically, the main difference is the non-linear relationship between knee angle and spring displacement, giving a non-linear torque-angle relationship.	12
9	Extension spring implementation in Simscape. As can be seen, the spring is connected between the appropriate points (output frames) of the thigh and shank spine, and in parallel to the knee motor model, which contains the knee joint.	12
10	Torque-speed characteristics of the motor.	13
11	The manipulator corresponding to a vertical one leg jump.	14
12	Vertical Paw velocity as a function of knee angle.	15
13	Linear regression fit of the pendulum data.	18
14	Comparison of normal and symmetric leg configurations	20
15	Initial poses for different link length ratios	20
16	An overview of the leg CAD model with a torsional spring.	21
17	An overview of the CAD model of the leg design, but showing only the components that will be manufactured inhouse. Axel that will be threaded and screwed directly into the motor shaft, and lead directly into a ball bearing, is emphasized in red. .	22
18	A 3D printed version of the leg thigh with the torsional spring.	22
19	Comparison of extension spring configurations: outside (left) and inside (right) the leg.	23
20	Linear regression fit of the pendulum data for the knee motor. Derived theta dot dot is the double derivative of the pendulum angle.	24
21	Linear regression fit of the pendulum data for the hip motor.	24

22	Grid search results showing jump height performance across different link length configurations under Earth gravity.	25
23	Grid search results showing jump height performance across different link length configurations under Mars gravity.	26
24	Commanded and actual hip joint angle achieved during the hip motor strength test simulation.	26
25	Torque output of the hip motors during the hip motor strength test simulation.	27
26	Knee speed until takeoff with A80BHP-H motor.	27
27	A06CLS V2 Motor Information (Curt)	31
28	A35CHM Motor Information	32
29	A80BHP-H Motor Information	32

List of Tables

2	Dimensions and density of the rigid bodies in the robot model. L1 and L2 have no set size, but are the variables we intend to optimize over.	10
3	Mass and inertia properties of the rigid bodies in the robot model. A list of the Eurepus robot's electronics can be found in [1].	11
4	Masses and dimensions used in the main body mass calculation.	11
5	Selected Motors	23
6	Best performing link length configurations and their corresponding jump heights for Earth and Mars gravity.	25

Abbreviations

Abbreviation	Description
TODO	To be filled in

1 Introduction

1.1 Motivation

The exploration of extraterrestrial environments represents one of the most demanding frontiers of robotic systems, requiring exceptional autonomy, resilience, and adaptability to navigate complex and unpredictable terrain. On Mars, wheeled rovers have proven their utility, with six successful deployments to date [17], robots like Axel [8] and Reachbot [9] have also been designed, tailored towards specific tasks. One such task that has received much attention in recent years, is the exploration of potential Martian and Lunar lava tubes [2]. These tubes are hollow caverns hypothesized to exist beneath the surface of Mars and the Moon, formed by ancient lava flows. They are of particular interest to astrobiologists and planetary scientists, as they could provide shelter from cosmic radiation and micrometeorites, as well as stable temperatures and access to subsurface water ice [2].

The exploration of such lava tubes present a unique challenge to robotic systems, as they are believed to be characterized by rough, uneven terrain, sharp rocks, and steep slopes. This could present a challenge to traditional wheeled rovers. Further, the motion of wheeled robots is limited to the ground plane, and thus, inherently, they do not utilize the lower gravity of extraterrestrial objects such as asteroids, the Moon and Mars. Jumping quadrupeds, on the other hand, inherently utilize the lower gravity of such objects, and in low earth gravity could potentially jump to heights of several meters [11]. This could allow them to traverse obstacles that would be insurmountable to wheeled rovers, such as steep slopes, large rocks, and gaps in the terrain.

While recent years have seen great progress in the development of quadruped robots, most quadrupeds still struggle with jumping in earth gravity TODO: CITE. Since, additionally, low gravity environments are very hard to replicate on earth, it is difficult to test hardware and control algorithms intended for quadrupeds jumping in low gravity. Jumping also includes high velocity impacts, making damage to the often expensive hardware likely. This motivates the main goal of this project, which is to develop a design for a small, lightweight, and low-cost jumping quadruped robot. The robot's low weight is intended to reduce the risk of damage during testing, and the low cost to make it more accessible to researchers, as well as reduce the cost of potential damage. Special emphasis is placed on being able to jump long distances, without losing the general utility of the quadruped form factor, such as the ability to walk on rough terrains, flexibly adjust body pose, and potentially carry scientific payloads.

1.2 Scope

As described in the Motivation section, section 1.1, the main goal of this project is to develop a design for a small, lightweight, and low-cost jumping quadruped robot. The work presented in this report is part of a specialization project, TTK4550 - Engineering Cybernetics, Specialization Project TODO: CITE, pursued at the Norwegian University of Science and Technology (NTNU), as a preparation for a master's thesis. So while the scope of the specialization project is limited to the development of a design, the overall goal is for the design to be used as the basis for a master's thesis, where the robot will be built and tested. The master's thesis will also include the development of control algorithms for the robot, which is not included in this report.

More precisely, the scope of this project is limited to the following:

-
- Developing a simplified simulation for the robot in MATLAB/Simulink, to be used for verification and evaluation of various design choices.
 - Choosing a specific method of actuation, such as motors, parallel torsional springs, parallel extension springs, or a combination of these.
 - Identifying key hardware components, such as motors and springs.
 - Designing a CAD model for a single leg of the robot. The leg must adhere to geometric and mechanical constraints such as:
 - Accommodating chosen springs and motors.
 - Being easily manufacturable using 3D printing and the CNC facilities readily available at NTNU.
 - Sturdiness, ie. being able to withstand the forces and impacts of jumping.

1.3 Related Work

The problem of robotic jumping in earth and low gravity environments has been studied by several researchers, with various approaches taken. One unique example is the Olympus robot [10] [11] developed by NTNU's ARL (Autonomous Robots lab), which uses a 5-bar linkage spring assisted leg to jump. The robot weighs TODO kg, is capable of jumping to heights of up to TODO meters in earth gravity, and has been tested in simulated low gravity environments. Another example is the 600g robot RAVEN (Robotic Avian-inspired Vehicle for multiple ENvironments) [13] developed at EPFL, which uses its bird-inspired 2 DOF multifunctional legs to jump rapidly into flight, walk on the ground, and hop over obstacles and gaps similar to the multimodal locomotion of birds. Notable for RAVEN is its geared BLDC motors, which wind up embedded torsional springs, which then assist in jumping. Apart from the different topology of the legs and springs, the concept is quite similar to that of Olympus. The RAVEN robot can jump TODO (26 cm) cm in earth gravity. A third example is the Grillo robot [12], which weighs 15g and takes off at velocities of about 30 body lengths per second, ie. 1.5m/s.

2 Theory

2.1 Actuator Modeling

2.1.1 DC Motor Model

2.1.2 BLDC Motor Model

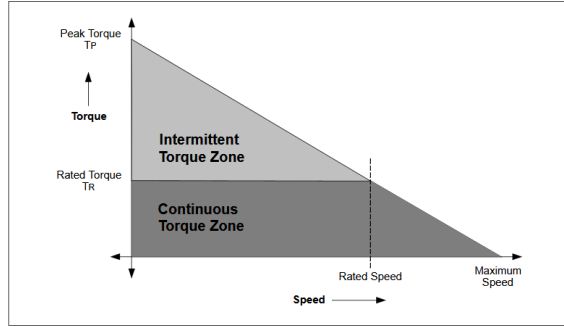


Figure 1: Torque-speed characteristics of a BLDC motor. TODO: Replace with an image that isn't stolen, and that we are allowed to use.

2.1.3 Gear Transmission Friction Model

Although electric motors for robotics are available for a wide power range, they are often too high speed and low power to do any useful work. For this reason, it is often necessary to use a gear transmission to increase the torque and reduce the speed of the motor.

In the presence of a geared transmission, assuming no power loss, the output torque and velocity of a geared motor are given by equation 1 and equation 2, respectively, where N is the gear ratio, τ_{in} is the input torque, τ_{out} is the output torque, w_{in} is the input velocity, and w_{out} is the output velocity [6].

$$w_{out} = \frac{w_{in}}{N} \quad (1)$$

$$\tau_{out} = N\tau_{in} \quad (2)$$

In reality, however, there is always some power loss in the transmission. A common way to model this is to use friction model consisting of a viscous friction term and a Coulomb friction term [6]. The viscous friction term is proportional to the velocity of the transmission, and the Coulomb friction term is a constant friction torque that must be overcome before the transmission starts moving. The total friction torque is the sum of these two terms, as seen in equation 3. It is also possible to drop one or the other of these terms, depending on the application [6].

$$\tau_{friction} = b_{viscous}\dot{\theta} + b_{coulomb}\text{sign}(\dot{\theta}) \quad (3)$$

In addition to friction, heavily gearing motors can lead to a very high apparent rotor inertia. If one looks at equation 4, it is clear that the apparent rotor inertia is proportional to the square of the gear ratio [6]. This can lead to a very high apparent rotor inertia, which can often be problematic to robotic applications. This is especially the case for cases with contact forces, as the high apparent rotor inertia can lead to very stiff and damaging collisions [16].

$$K = \frac{1}{2}I_{rotor}(G\dot{\theta})^2 = \frac{1}{2}I_{rotor}G^2(\dot{\theta})^2 = \frac{1}{2}I_{apparent}(\dot{\theta})^2 \quad (4)$$

2.2 Spring Modeling

Springs are mechanical devices that store and release energy when subjected to displacement. There are two main types of springs: extension springs and torsion springs.

Extension springs are designed to operate with a tension load, meaning they extend as the load is applied. The force exerted by an extension spring is proportional to the displacement from its equilibrium position, following Hooke's Law, which is given by:

$$F = -kx \quad (5)$$

where F is the force exerted by the spring, k is the spring constant, and x is the displacement from the equilibrium position. The potential energy stored in an extension spring is given by:

$$U = \frac{1}{2}kx^2 \quad (6)$$

Torsion springs, on the other hand, are designed to operate with a rotational or twisting load. They exert a torque that is proportional to the angular displacement from their equilibrium position. The torque generated by a torsion spring is given by:

$$\tau = -k\theta \quad (7)$$

where τ is the torque, k is the torsion spring constant, and θ is the angular displacement. The potential energy stored in a torsion spring is given by:

$$U = \frac{1}{2}k\theta^2 \quad (8)$$

Both types of springs are widely used in various mechanical systems to provide force or torque, absorb shock, and store energy.

2.3 Kinematics, Jacobians, and Virtual Work

2.3.1 Robot Kinematics

Consider a robotic link arm existing in \mathbb{R}^2 consisting of n links, each with a length l_i and a joint angle q_i . The position of the end-effector is given by the vector $\mathbf{x} = [x, y]^T$, where x and y are the coordinates of the end-effector in the global coordinate system. Using simple trigonometry, the position of the end-effector can be expressed as a function of the joint angles and link lengths as seen in equation 9. Axes and joint angles corresponding to the expression in equation 9 can be seen in figure 2.

$$\mathbf{x} = \begin{bmatrix} x \\ y \end{bmatrix} = \begin{bmatrix} \sum_{i=1}^n l_i \cos(q_i) \\ \sum_{i=1}^n l_i \sin(q_i) \end{bmatrix} \quad (9)$$

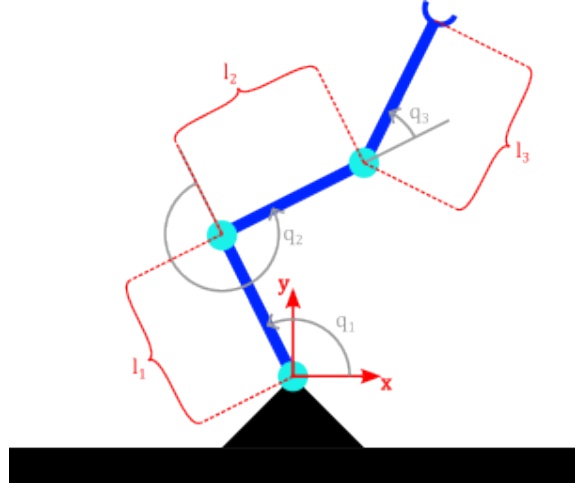


Figure 2: Illustration of a 3 link robotic link arm in \mathbb{R}^2 with n links.

2.3.2 Jacobian Matrix

As described in section 2.3.1, the position of the end-effector can be expressed as a function of the joint angles and link lengths. In robotics, it is often useful to express the relationship between infinitesimal changes in the joint angles and the resulting change in the end-effector position. As can be seen in equation 10, infinitesimal changes in variables δy and δx can be described by means of the partial derivative [3]. If this is compared to the definition of the jacobian in equation 11, it is clear that the jacobian matrix \mathbf{J} can be used to map infinitesimal changes in joint angles to changes in the end-effector position, as illustrated in equation 12. The limit of an infinitesimal change over an infinitesimal time interval is a derivative, and thus by dividing each side in equation 12 by δt , one arrives at the expression in equation 13, by which the jacobian can be used to map joint velocities to end-effector velocities.

$$\delta y = \frac{\partial y}{\partial x} \delta x \quad (10)$$

$$\mathbf{J} = \begin{bmatrix} \frac{\partial x}{\partial q_1} & \frac{\partial x}{\partial q_2} & \dots & \frac{\partial x}{\partial q_n} \\ \frac{\partial y}{\partial q_1} & \frac{\partial y}{\partial q_2} & \dots & \frac{\partial y}{\partial q_n} \end{bmatrix} \quad (11)$$

$$\delta \mathbf{x} = \mathbf{J} \delta \mathbf{q} \quad (12)$$

$$\dot{\mathbf{x}} = \mathbf{J} \dot{\mathbf{q}} \quad (13)$$

2.3.3 Force/Torque Mapping

Consider a general robotic manipulator, such as the one illustrated in figure 2, but with an arbitrary amount, n , of joints and links. Using the principle of conservation of power, one arrives at the formulation found in equation 14.

$$\text{power at the joints} = (\text{power to move the robot}) + (\text{power at the end-effector}) \quad (14)$$

As the power used to move the robot approaches zero, ...

Consider a robotic manipulator with n joints, each with a joint angle q_i and a joint torque τ_i . The position of the end effector for such a system is given by equation 9, and thus the formula in equation 13 can be used to map joint velocities to end effector velocities.

TODO: Derive equation 15 by either power balance, or virtual work.

$$\tau = J^T F \quad (15)$$

2.4 Contact Friction

TODO

2.5 Numerical Solvers

Although a detailed review of numerical solvers and the associated theory is beyond the scope of this theory section, it is worth mentioning that numerical simulation of contact dynamics is particularly challenging. This is due to the discontinuities and high-frequency events that occur during contact. These dynamics often require the use of stiff solvers to accurately capture the rapid changes in forces and velocities [4][14]. Stiff solvers are designed to handle problems with widely varying timescales, ensuring stability and accuracy in the simulation of contact events. Without the use of stiff solvers, simulations can become unstable or fail to converge, leading to inaccurate results. Examples of stiff solvers include the well known ode15s and ode23s solvers in MATLAB, which are specifically designed to handle stiff ordinary differential equations [15].

2.6 Linear Least Squares Regression

Linear least squares regression is a method for finding the best-fitting line through a set of points by minimizing the sum of squared residuals. Given a set of observations (x_i, y_i) and a linear model $y = X\beta$, where X is the matrix of input variables and β contains the model parameters, the residual r_i for each observation is:

$$r_i = y_i - X_i\beta$$

The sum of squared residuals S is then:

$$S = \sum_{i=1}^n r_i^2 = (y - X\beta)^T (y - X\beta)$$

To minimize S , we take its derivative with respect to β and set it to zero:

$$\frac{\partial S}{\partial \beta} = -2X^T(y - X\beta) = 0$$

Solving for β yields the normal equations:

$$X^T X \beta = X^T y$$

The solution is therefore:

$$\beta = (X^T X)^{-1} X^T y$$

This solution minimizes the sum of squared residuals and provides the optimal parameters β in the least squares sense.

2.7 Inverse Kinematics

Inverse kinematics solves for joint angles that achieve a desired end-effector pose. For a planar two-link manipulator with link lengths L_1 and L_2 , given a desired end-effector position (x, y) , the joint angles θ_1 and θ_2 can be found analytically.

From the law of cosines, θ_2 is:

$$\theta_2 = \pm \arccos\left(\frac{x^2 + y^2 - L_1^2 - L_2^2}{2L_1L_2}\right)$$

The angle θ_1 is then:

$$\theta_1 = \arctan 2(y, x) - \arctan 2(L_2 \sin(\theta_2), L_1 + L_2 \cos(\theta_2))$$

The \pm in the equation for θ_2 indicates that two solutions exist for most end-effector positions - one with the second joint angle positive and one negative. When $L_1 = L_2$, a singularity occurs at $(0, 0)$ where infinite solutions exist. At the workspace boundary where $x^2 + y^2 = (L_1 + L_2)^2$, only one solution exists.

3 Modeling and Simulation

For the purpose of doing design verification and optimization, a simplified model of the robot was created. The model was created in Simscape, a physical modeling toolbox integrated with MATLAB/Simulink.

3.1 Simscape

Simscape is a simulation tool that allows you to rapidly create models of physical systems within Mathworks' MATLAB/Simulink environment. With Simscape, physical systems are built by interconnecting blocks representing physical components, such as rigid bodies, joints and springs in a block diagram. The blocks are parameterized by physical properties, such as mass, inertia, and damping. Simscape automatically generates the equations of motion for the system, which can be solved numerically to simulate the system's behavior. Like you can do with Simulink without Simscape, you can also add ordinary Simulink blocks, including Matlab Function blocks, to the model. Simscape is also compatible with Simulink's multiple numerical solvers, such as ode15s, ode45, and ode23s.

An example of a typical SimScape block diagram can be found in figure 3. A visualization of the corresponding model can be seen in figure 4. As one can see, each element in a block diagram is typically either a rigid body, or joints connecting the various rigid bodies. Since a given body has multiple possible locations that a joint could be connected to, as well as axes it can act on, blocks can export different frames, with different origins and orientations, depending on the desired position and orientation of the joint. For example, for a block representing the robotic equivalent of a thigh, natural output frames would be the ones with origins at the top and bottom of the thigh, with a select axis aligned with the desired knee or hip axis of rotation. TODO: We want to use something other than the tutorial here, but our robot model is too split into submodels of submodels, so it loses the intuition you get from a "flatter" model. Will fix later.

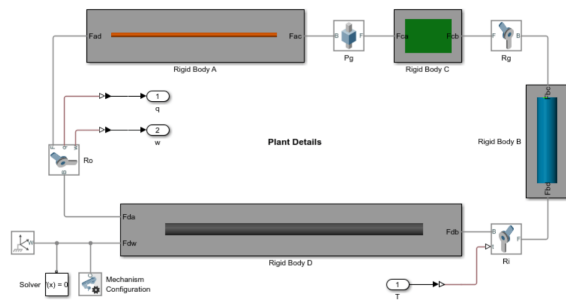


Figure 3: A typical Simscape block diagram.

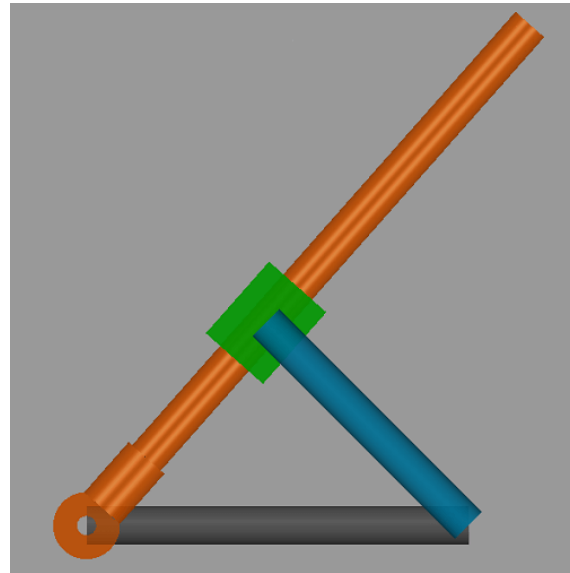


Figure 4: A visualization of the model in figure 3.

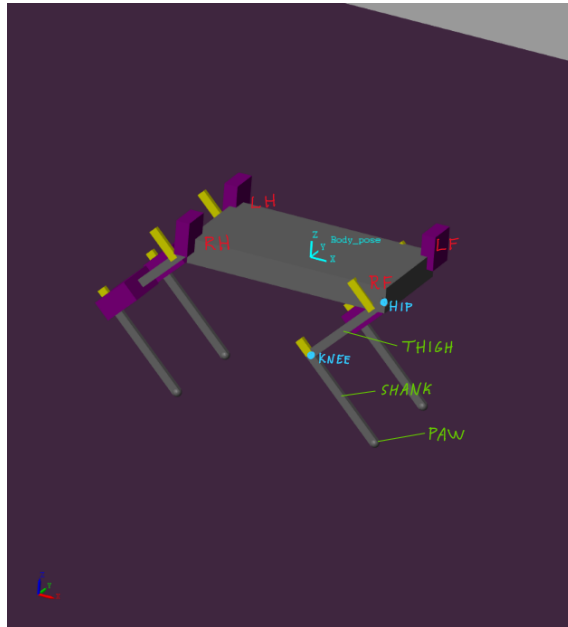


Figure 5: Naming conventions for the parts of the robot, as well as forwards direction definition.
TODO: name spines

3.2 Rigid Body Components of the Robot Model

Since the purpose of the Simscape model is not to facilitate the development of a complicated full degree of freedom feedback controller, nor to optimize every small detail of the design, a simplified model was selected. This model consists of a main body with four legs, each of which with two degrees of freedom. A visualization of the model, as well as an overview of the body's naming conventions can be found in figure 5. An overview of the body's angle conventions can be found in figure 6. Note the absence of a hip abduction/adduction joint. This is because the model's main purpose is to verify the design for jumping in the sagittal (forward-backward and upwards-downwards) plane, and the hip abduction/adduction joint is not necessary for this purpose.

Regarding the naming conventions presented in figure 5, note especially the naming of the different legs corresponding to location on the body, namely RH (Right Hind), RF (Right Front), LH (Left Hind), and LF (Left Front). Note also the naming of the joints hip (HIP) and knee (KNEE). If you see the angle conventions in figure 6, you can see that the angles of these joints correspond to the angles θ_1 and θ_2 respectively. Note that an orientation of zero degrees for the hip joint corresponds to the leg pointing straight downwards, and an orientation of zero degrees for the knee joint corresponds to the shank pointing in the same direction as the thigh.

As can be seen in both figure 5 and figure 6, in addition to the main body and legs colored in grey, the robot model also contains large purple blocks. These blocks represent motor masses, and their mass can be adjusted to represent different motors. In the current figures, the hip motors are A06CLS V2 motors, and the knee motors are A80BHP-H motors.

3.3 Rigid Body Masses and Inertias

In Simscape, the mass and inertia properties of a rigid body can be specified by the user or automatically calculated based on the body's geometry and material properties. Hybrid solutions are also possible, where the user specifies some properties and Simscape calculates the rest [7].

In the case of this model, a summary of the origin of the mass and inertia properties of the rigid bodies can be found in table 3. Exceptions are the properties of the main body and the paws, which will be specified in more detail in the two next paragraphs. For the parts whose mass and

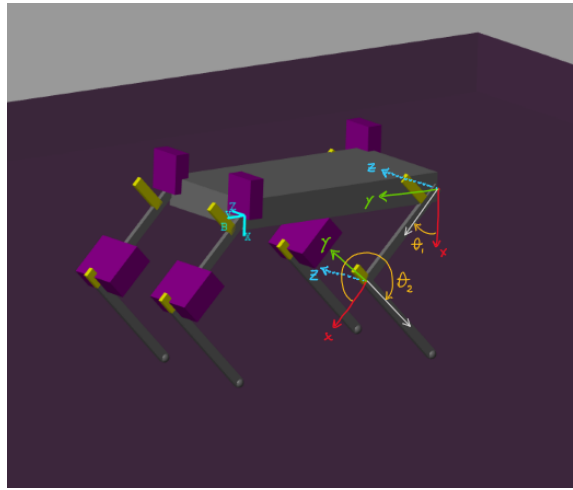


Figure 6: Angle conventions for the robot body.

Component	Dimensions (cm)	Density (kg/m ³)	Mass (g)
Thigh	L1 x 0.5 x 0.25	2700	Calculated
Shank	L2 x 0.5 x 0.25	2700	Calculated
Hip Motor (A06CLS V2)	2 x 0.8 x 1.78	Calculated	7g
Knee Motor (A20BHM)	2.3 x 1.2 x 2.75	Calculated	20g
Knee Motor (A80BHP-H)	4.0 x 2.0 x 3.75	Calculated	79g
Thigh Spine	2 x 0.5 x 0.25	2700	Calculated
Shank Spine	1 x 0.5 x 0.25	2700	Calculated

Table 2: Dimensions and density of the rigid bodies in the robot model. L1 and L2 have no set size, but are the variables we intend to optimize over.

inertia are calculated by the geometry, a summary can be found in table 2.

The mass properties of the main body are based on the hardware components used by the Eurepus robot constructed by Maurer and El Agroudi [1]. Since early in the design process a rough estimate was needed for the robot body mass, and it seemed likely that the electronic solution, apart from the motors, would be similar to the Eurepus robot, an approximate mass of the main body was calculated based on the mass of some of the Eurepus robot's electronics plus an approximate amount of Nylon body material, four motors, and a random chosen microcontroller (MCU) mass. The formula used for the approximate of the main body mass can be found in equations 16 to 18. The masses corresponding to variables in equations 16 to 18 can be found in table 4. The motor mass chosen in table 4 corresponds to the mass of the AGF-RC A20BHM motor. This motor was chosen because, although the current plan is to use the A06CLS V2 motor, which is lighter, we would rather overestimate the mass of the main body than underestimate it, and a change of motor is one of the more likely changes to the robot design, as well as one of the changes that would increase the mass of the robot the most. TODO: Add method used for the inertia as well.

The geometrical, mass and inertia properties of the paws differ based on which of two scenarios we intend to simulate. The first scenario is the normal jumping scenario, in which the paw mass is simply set to 1000 kg/m³, though choosing the actual density of rubber would maybe be more appropriate. The dimensions of the paw are in this scenario simply chosen so that the diameter coincides exactly with $\max(\text{shank width}, \text{shank height})$. The second scenario is the one described in section 4.5, where the paw mass and volume is increased to estimate hip flexor/extensor motor requirements.

$$m_{plate} = \rho_{nylon} \cdot V_{plate} = \rho_{nylon} \cdot l_{plate} \cdot w_{plate} \cdot h_{plate} \quad (16)$$

Component	Mass	Density (kg/m ³)	Inertia	Geometry
Main Body	See section 3.3	See section 3.3	See section 3.3	Rectangular Prism
Thigh	From geometry	2700 (Aluminium 6061)	From geometry	Rectangular Prism
Shank	From Geometry	2700 (Aluminium 6061)	From Geometry	Rectangular Prism
Law	From Geometry	2700 (Aluminium 6061)	From Geometry	Rectangular Prism
Hip Motor	Actual motor mass	From Geometry	From Geometry	Rectangular Prism
Knee Motor	Actual motor mass	From Geometry	From Geometry	Rectangular Prism
Thigh Spine	From Geometry	2700 (Aluminium 6061)	From Geometry	Rectangular Prism
Shank Spine	From Geometry	2700 (Aluminium 6061)	From Geometry	Rectangular Prism
Paw	See section 3.3	See section 3.3	See section 3.3	Sphere

Table 3: Mass and inertia properties of the rigid bodies in the robot model. A list of the Eurepus robot’s electronics can be found in [1].

Variable	Description	Value
ρ_{nylon}	Density of Nylon	1520 kg/m ³
l_{plate}	Length of the plate	10 cm
w_{plate}	Width of the plate	6 cm
h_{plate}	Height of the plate	1.67 cm
$m_{battery}$	Mass of the battery	27 g
m_{motor}	Mass of one motor	20 g
m_{I2C}	Mass of the I2C module	5.1 g
m_{ADC}	Mass of one ADC module	2.4 g
m_{PWM_driver}	Mass of the PWM driver	8.5 g
m_{MCU}	Approximate mass of some microcontroller	30 g
m_{main_body}	Resultant mass of the main body	332 g

Table 4: Masses and dimensions used in the main body mass calculation.

$$m_{eurepus_electronics} = m_{battery} + m_{I2C} + 12 \cdot m_{ADC} + m_{PWM_driver} \quad (17)$$

$$m_{main_body} = m_{plate} + m_{eurepus_electronics} + m_{MCU} + 4 \cdot m_{motor} \quad (18)$$

3.4 Elastic Components: Springs

In addition to the model’s many rigid bodies, we also implemented two different forms of spring based passive actuation, namely:

- **A torsional spring** acting in parallel with the knee joint, as illustrated in figure 7. This spring is at zero extension when the knee joint is at zero degrees, and applies a torque that is proportional to the knee joint angle, as covered in section 2.2.
- **An extension spring** acting in parallel with the knee joint, attached to the shank and thigh spine, as illustrated in figure 8. The force generated by the extension spring is proportional to its displacement, as covered in section 2.2. The spring is intended to be unloaded when the knee joint is at zero degrees.

The torsion spring was implemented in the model using Simscape’s prismatic joint option to add spring stiffness. The extension spring, on the other hand, was connected in parallel to the joint using Simscape’s natural block diagram functionality, as seen in figure 9.

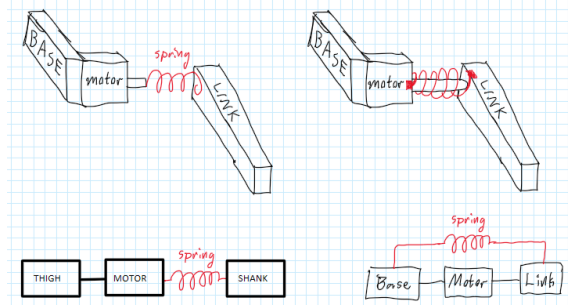


Figure 7: A figure displaying the conceptual difference between a parallel spring (right), as used in this work, and a series elastic spring (left) as used in the ANYmal robot [5].

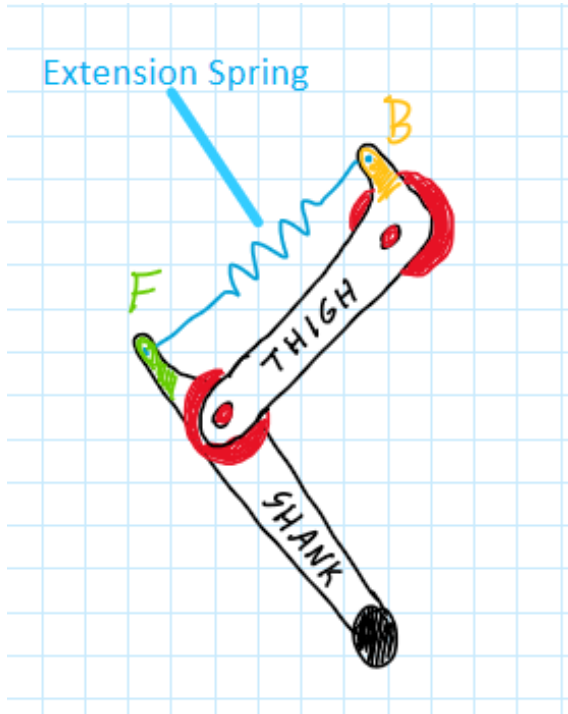


Figure 8: A figure displaying the concept of a parallel extension spring, note that the spring generates torque directly in parallel with the knee joint just like for the parallel torsional spring seen in figure 7. Mathematically, the main difference is the non-linear relationship between knee angle and spring displacement, giving a non-linear torque-angle relationship.

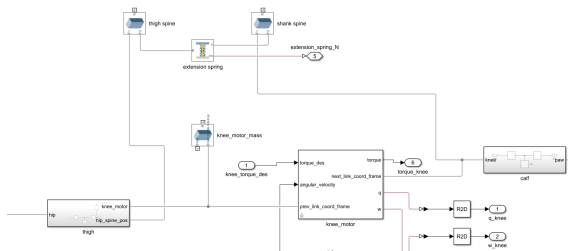


Figure 9: Extension spring implementation in Simscape. As can be seen, the spring is connected between the appropriate points (output frames) of the thigh and shank spine, and in parallel to the knee motor model, which contains the knee joint.

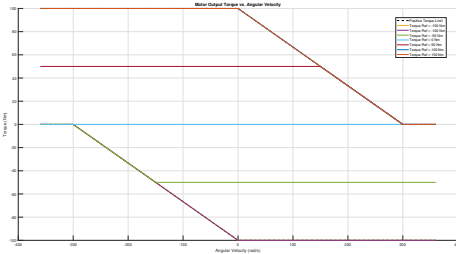


Figure 10: Torque-speed characteristics of the motor.

3.5 Motor Modeling

To be able to more accurately judge the jumping capability of different motors, a motor model in the form of a torque speed curve was implemented. The BLDC torque-speed curve presented in figure 1 is characterized by four parameters, namely the stall torque, the operating torque, the rated speed, and the maximum speed. Since motor suppliers contacted (primarily agf-rc and T-motor) were unable to provide most of the desired parameters, we chose a motor model with only two parameters, namely stall torque and maximum speed. The torque-speed model thus became a simple model where torque decreases linearly from stall torque, at speeds smaller than or equal to zero, to zero at speeds greater than or equal to maximum speed. The model is identical for negative velocities and torques, but with opposite signs. An example of the relation between desired torques and achieved torques for a given motor max speed can be seen in figure 10.

3.6 Solver selection

As described in section 2.2, the potential energy of a loaded spring can be easily calculated. Similarly, the potential energy due to gravity of a robot at the peak of a jump can also be determined. For the reasons discussed in section 2.5 we chose a stiff numerical solver, initially, we chose the ode15s solver. However, it was eventually observed that simulations using ode15s occasionally resulted in jump trajectories where the gravitational potential energy at the robot's peak height exceeded the combined potential energy of the four fully loaded springs by a factor of 2, even for jumps with only passive (spring) actuation. To address this inaccuracy, we experimented with different numerical solvers and ultimately selected the ode23s solver. This solver provided accurate simulations without artificially generating excess energy, and it performed efficiently.

4 Robot Design

4.1 The Single Vertical Manipulator Jump Model

In the absence of air resistance, which is negligible for a robot like this during a jumping maneuver like this, the factor that determines jumping distance is body velocity at takeoff. To keep things simple, in the following will be given an example where the sole goal is to maximize vertical jump height. Further, only a one leg robot with a 2 DOF leg with equal link lengths is considered.

For a robot such as the one described above, the position of the paw relative to the body can be described by the standard 2 link manipulator equation as seen in equation 19, in accordance with the theory in section 2.3.1. For this simple robot, it is assumed that the optimal jump is one where the body center of mass and paw position move in opposite directions, with velocities strictly along the up/down y axis. This example is illustrated in figure 11. As is obvious from the figure and from the kinematics, for such a jump $\theta_1 = -\frac{(\theta_2 + \pi)}{2}$, and $\dot{\theta}_2 = -2\dot{\theta}_1$. If this is combined with the jacobian for the end effector, given in equation 4.1, one can plot the vertical velocity of the paw as a function of the knee angle θ_2 , this is shown in figure 12. This is done using the jacobian as in

equation 13.

As can be seen in figure 12, the joint velocity of the leg much more readily translates to body velocity when the knee is crouched. Without giving a detailed derivation, the intuition meant to be gained from figure 12 is that how quickly the leg joints are accelerated can be just as important as the speed it is accelerated to. This has an important interpretation for the choice of motors, in the sense that, if a given motor is unable to accelerate the leg joints quickly enough, there is little sense in looking for a faster motor, unless it is also stronger.

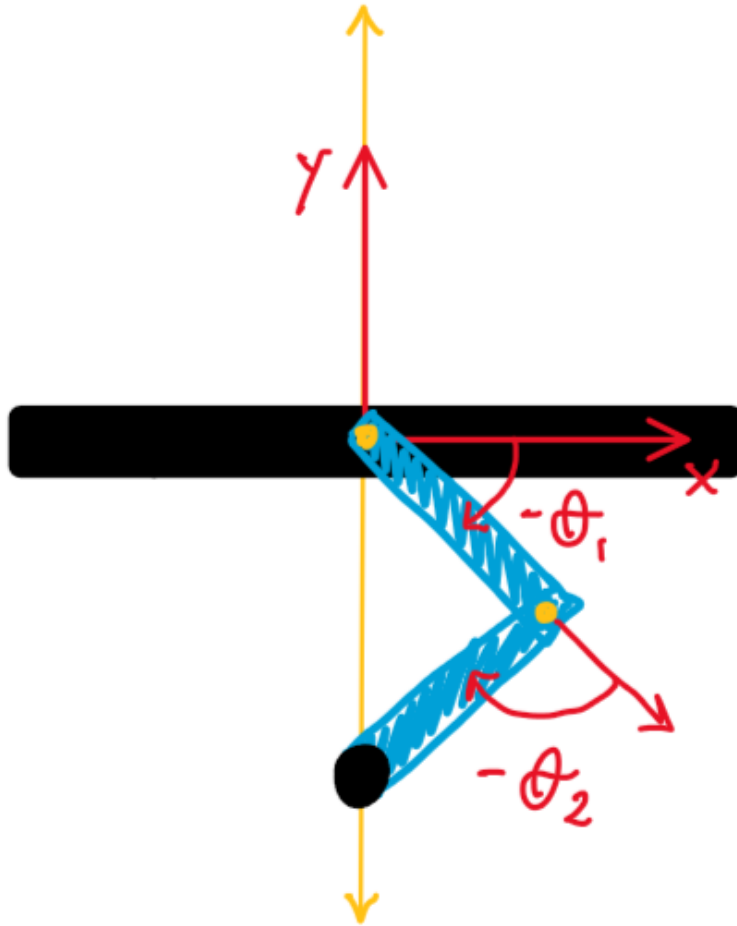


Figure 11: The manipulator corresponding to a vertical one leg jump.

$$\begin{aligned} x_{\text{end}} &= L_1 \cos(\theta_1) + L_2 \cos(\theta_1 + \theta_2) \\ y_{\text{end}} &= L_1 \sin(\theta_1) + L_2 \sin(\theta_1 + \theta_2) \end{aligned} \quad (19)$$

$$J = \begin{bmatrix} -L_1 \sin(\theta_1) - L_2 \sin(\theta_1 + \theta_2) & -L_2 \sin(\theta_1 + \theta_2) \\ L_1 \cos(\theta_1) + L_2 \cos(\theta_1 + \theta_2) & L_2 \cos(\theta_1 + \theta_2) \end{bmatrix}$$

4.2 Actuation Method Selection: Motors Only

Initially, experiments were done utilizing motors alone. Due to the need for a light and strong motor, initially a series of AGF-RC motors were looked at, due to their high torque to weight ratio. As covered in section 3.5, a motor model consisting of a stall torque and a max velocity, with a linear decrease in max torque between these two, was chosen. For the AGF-RC motors, their

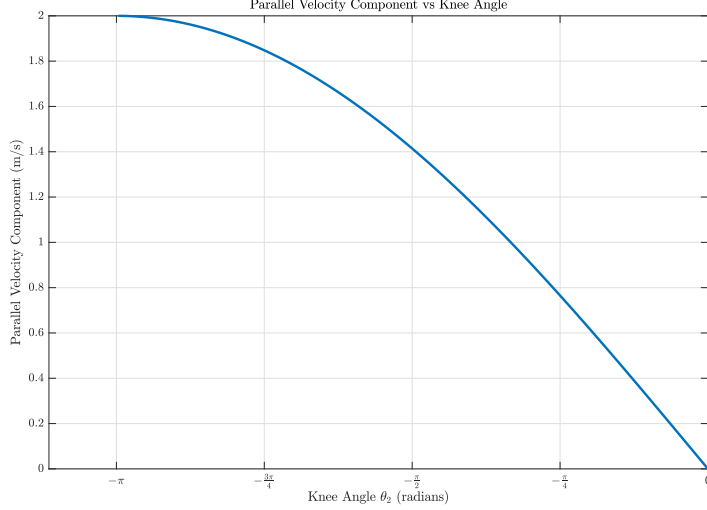


Figure 12: Vertical Paw velocity as a function of knee angle.

provided stall torque and operating speed were used for the motor model parameters. Attempts were made to get more information about the motors' performance characteristics, but the supplier, AGF-RC, was unable to provide more detailed information. While extensive testing was done with various motors, the jumping performance was so far from acceptable that the idea was abandoned, and the full scope of the experiments are considered outside the scope of this report.

More details about the results of the motor only jumps can be found in section 8.4, but a brief overview of the reasoning involved will be given here. The most relevant of the motors chosen for these experiments was the A80BHP-H motor by AGF-RC, which was chosen because it had both the highest stall torque and operating speed of all the AGF-RC motors. Info about the A80BHP-H motor can be found in appendix D. Attempts were made to identify motors in the same weight range with similar stall torques and operating speeds, but none were found. The experiments using the A80BHP-H were therefore, to a certain degree, considered an "optimistic estimate". Since no satisfactory results were achieved with the A80BHP-H motor, as discussed in section 8.4, it was decided to explore alternatives to motor-only actuation.

The tests with the A80BHP-H motor were done by providing the knee motors with reference torques equal to their max torque, with the motor model limiting the resultant torque to more realistic values. Meanwhile, the hip joints were actuated according to the control law seen in equation 23 to limit slipping. This control law is based on equation 15, as derived in section 2.3.3, combined with the theory on friction presented in section 2.4. Equation 15 is derived with an assumption of zero velocity/equilibria (TODO), an assumption that is obviously not valid for this dynamic jumping scenario. Despite this, very little slipping is observed in practice.

$$N = \text{Normal force} \quad (20)$$

$$\mu = \text{friction coefficient} = 0.8 \quad (21)$$

$$\tau_{\text{friction cone limit}} = J^T \begin{bmatrix} N\mu \\ 0 \end{bmatrix} \quad (22)$$

$$\max(|\tau_{knee}|) = \tau_{\text{friction cone limit}} \quad (23)$$

Using this control law, jumping for variously dimensioned robots were attempted. As covered in section 8.4, none of them were satisfactory. Tests were eventually terminated, as no leg and body link length configuration was capable of jumping satisfactorily. By satisfactorily, it is meant that the robot center of mass cleared the ground by a distance more than twice that of the leg length, ie., if the legs are 20cm long, the center of mass should clear the ground by at least 40cm.

For comparisons between this motor-only jumping and later spring+motor jumping, it is worth mentioning that the spring-motor jumping is done not with the A80BHP-H motors, but with weaker and slower motors, as well as with more realistic motor friction models. The reason the A80BHP-H motors were not used for the spring-motor jumping simulations, is that the motor supplier's website (AGF-RC) stated an operating travel range of 90 degrees. This was assumed to be correct, as other AGF-RC motors with stated operating ranges of 180 degrees have had actual mechanical limits of 220 degrees, so such a limitation was not considered out of the ordinary. For that reason, the motors initially purchased were not the A80BHP-H motors, and they are therefore not used for the rest of the experiments in this report. Later consultations with the supplier's website revealed conflicting information regarding the operating range of the A80BHP-H motor, and direct contact with the supplier revealed that the motor is in fact not limited to 90 degrees of travel. For this reason, potential use of the A80BHP-H motor for the spring-motor jumping is discussed in the future work section, section 10.1.

4.3 Actuation Method Selection: Motors and Torsional Spring

The next actuation method considered was to use a combination of motors and torsional springs, as this is the design we ended up choosing, a CAD model of this design can be seen in figure 16. With this design, the knee motors are used to compress the torsional springs, once the knee joint reaches a desired angle, ie. has stored the desired amount of energy, the motors are turned off, and the springs accelerate the legs' joints quickly enough for the robot to take off. Results from simulations are presented in section 8.2, but in short, jumping performance is superior to that of the motor-only jumps. For the spring-motor jumps, a friction model as derived in section 5 was used. Again, note the much weaker motor used in

4.4 Actuation Method Selection: Motors and Extension Spring

In addition to the torsional spring design, attempts were made to design a leg utilizing an extension spring. The resulting design is shown in figure 19. Although experiments akin to the ones done for torsional springs were done with comparable results, the extension spring design was ultimately abandoned. The reason for this was pure geometrical constraints, which are discussed in section 7.2. Because the extension spring design was abandoned, the details surrounding the extension spring simulations and simulation results are considered outside the scope of this report.

4.5 Hip Motor Strength Requirements

While the main purpose of the designed robot is to be proficient at jumping, the inclusion of torsional knee springs as a major part of the actuation method, and the subsequent lessened importance of the hip motors for jumping, complicated the choice of hip motors. For a conservative bound on the torque and speed required for in air attitude stabilization [1] uses a heuristic of three 90-degree back-and-forth lateral swings per second as a benchmark. Although the purpose of our robot is not to do in-air attitude stabilization, this heuristic was partially utilized for verification that the hip motors were strong enough. More specifically, the robot body was fixed in space, and the robot's paws were set to be 1cm diameter spheres of iron (ie. with a density of $7800 \frac{kg}{cm^3}$, for a total mass of ≈ 32 g). The hip motor was then commanded to follow a trajectory according to the heuristic specified in [1]. The results of this simulation are presented in section 8.3. While the paw masses used in [1] were 80g, the Eurepus robot's main body mass was also closer to 800g, compared to our body mass of approximately 300g. Our experimental paw masses of 32g were therefore considered appropriate, considering attitude stabilization is not strictly speaking a goal for the robot.

5 Motor Friction Estimation

This section details the estimation of the motor friction coefficients using a pendulum model. The pendulum is used to measure the motor friction coefficients by measuring the angular velocity and acceleration of the pendulum as it is released from a known initial angle. The friction coefficients are then estimated using linear regression.

5.1 Pendulum Modeling

The pendulum used in the motor friction tests consists of an aluminum rod of length $l_{\text{arm}} = 0.19$ meters and a ballast mass $m_{\text{ballast}} = 0.301$ kg attached at a distance $r = 0.08$ meters from the pivot. The total mass of the arm is $m_{\text{arm}} = 0.034$ kg. The pendulum is modeled as a rigid body rotating about the motor shaft with a moment of inertia I given by:

$$I = \frac{1}{3}m_{\text{arm}}l_{\text{arm}}^2 + m_{\text{ballast}}r^2$$

The equation of motion for the pendulum, considering only viscous friction, is:

$$I\ddot{\theta} + b\dot{\theta} + (m_{\text{arm}}\frac{l_{\text{arm}}}{2} + m_{\text{ballast}}r)g \sin(\theta) = 0$$

where:

- θ is the angular displacement (positive counterclockwise, zero at vertical down position)
- $\dot{\theta}$ and $\ddot{\theta}$ are the angular velocity and acceleration, respectively
- b is the viscous damping coefficient
- $g = 9.81 \text{ m/s}^2$ is the acceleration due to gravity

5.2 Linear Regression Derivation

Rearranging the equation for linear regression purposes:

$$I\ddot{\theta} + (m_{\text{arm}}\frac{l_{\text{arm}}}{2} + m_{\text{ballast}}r)g \sin(\theta) = -b\dot{\theta}$$

This can be expressed in the form:

$$Y = X\beta$$

where:

- $Y = -I\ddot{\theta} - (m_{\text{arm}}\frac{l_{\text{arm}}}{2} + m_{\text{ballast}}r)g \sin(\theta)$,
- $X = \dot{\theta}$,
- $\beta = b$.

The angular velocity $\dot{\theta}$ and acceleration $\ddot{\theta}$ are computed using centered finite differences:

$$\dot{\theta}_i = \frac{\theta_{i+1} - \theta_{i-1}}{2\Delta t}$$

$$\ddot{\theta}_i = \frac{\theta_{i+1} - 2\theta_i + \theta_{i-1}}{(\Delta t)^2}$$

where Δt is the time step between measurements.

The linear least squares solution for β is given by:

$$\beta = (X^T X)^{-1} X^T Y$$

This yields the viscous damping coefficient b .

The viscous damping coefficient b is found to be 0.001 Nm/rad/s for the hip motors (A20 etc) and 0.0001 Nm/rad/s for the knee motors (A14 etc).

A plot of the data and the linear regression fit is shown in figure 13.

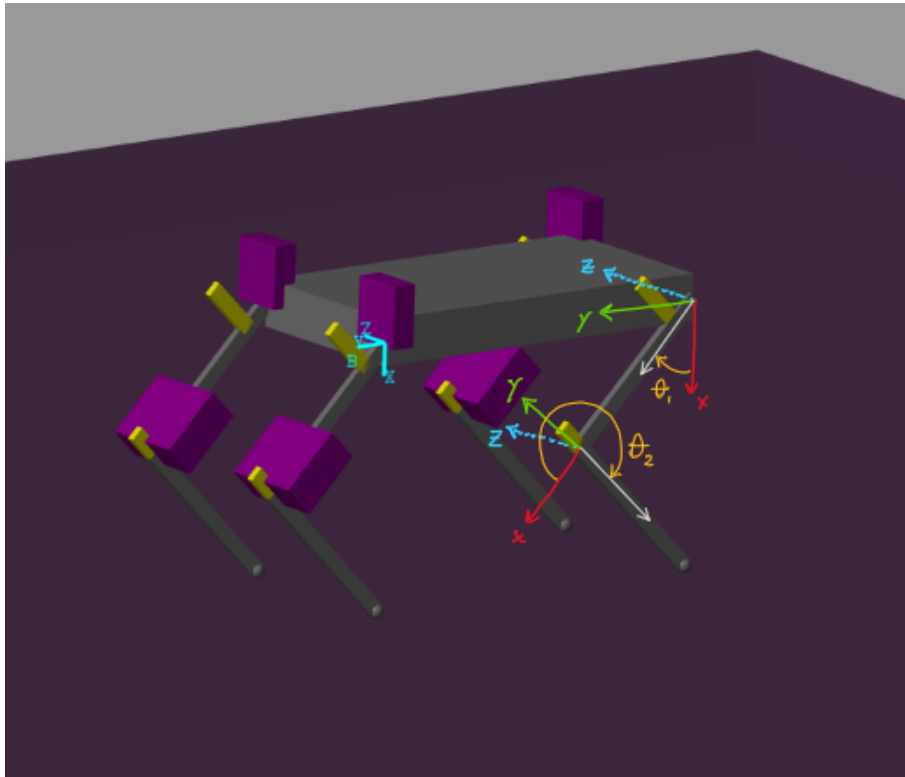


Figure 13: Linear regression fit of the pendulum data.

TODO: Switch figure 13 to the correct figure, I just want to compile for now.

6 Link Length Optimization

This section details the optimization of the robot's link lengths to maximize jumping performance. The optimization ensures the robot can achieve sufficient jump heights for future reinforcement learning (RL) control policy training and demonstration. A grid search approach using a simplified Simscape robot model systematically explores different link length configurations.

6.1 Problem definition

The link lengths and initial pose critically determine the robot's jumping capability due to the passive knee spring actuation. Link lengths constrain the possible initial poses for a given jumping angle, while the pose determines spring compression and thus available potential energy. Additionally, link lengths affect the center of mass trajectory during jumps, influencing how gravitational and ground contact forces impact the robot's movement. A grid search using a simplified Simscape model (detailed in section 3) identifies optimal link lengths.

6.2 Problem simplification

While the robot should jump both vertically and at angles to overcome obstacles, optimizing for angled jumps presents challenges. We want to directly compare the jumping performance of different link lengths, but it is not obvious how to place the initial pose of the robot to achieve any given jumping angle using only the passive actuation of the knee springs. This is a problem for future RL control policies.

To simplify the optimization, only the vertical jumping performance was considered, so that different link lengths can be compared directly. Vertical jumps are achieved across link lengths by flipping the front legs, such that the legs are symmetric by the vertical axis, as shown in figure 14. In this configuration, the movement of the legs during the jump is symmetric and the robot center of mass remains in the horizontal center of the robot, such that any horizontal component of the jump is canceled out. Though this is not the asymmetric leg configuration the robot will use in practice, it provides an approximation for the jumping performance of a given link length configuration. The metric used to evaluate the jumping performance is the maximum height reached by the center of mass of the robot body, minus the maximum standing height reached by the center of mass of the robot body when the legs are fully extended and the paws are in contact with the ground.

The asymmetric leg configuration can also achieve vertical jumps by adjusting the angle between the hip-to-paw vector and vertical, as shown in figure ???. However, finding or calculating the optimal offset for arbitrary link lengths is complex. We therefore simplify by placing paws directly beneath hips, except when $L_2 > L_1$. While this produces less realistic jump heights, it greatly simplifies optimization.

For $L_2 > L_1$ configurations, placing paws directly under hips results in near-vertical legs that slip during jumps. We prevent this by translating paws slightly inward (figure ??). This better approximates the practical asymmetric case where paws require similar translation for vertical jumps. To handle the increased opposing horizontal forces between paws in the symmetric configuration, we double the friction coefficients from 1.0/0.8 to 2.0/1.6 (static/kinetic), which further reduces slipping.

6.3 Initial Pose Calculation

For each set of link lengths, an initial pose must be calculated that satisfies several constraints:

The initial pose must satisfy four key constraints: the paws must maintain ground contact, knee angles must be maximized to store maximum spring potential energy, knees cannot penetrate the ground, and both knees bend outward rather than inward to avoid self-collision.

Due to the symmetric leg configuration, the initial pose is identical but flipped for both front and back legs, ensuring vertical jumps.

The pose calculation considers three cases based on link length ratios:

1. $L_1 = L_2$ (equal lengths)
2. $L_2 > L_1$ (longer lower link)

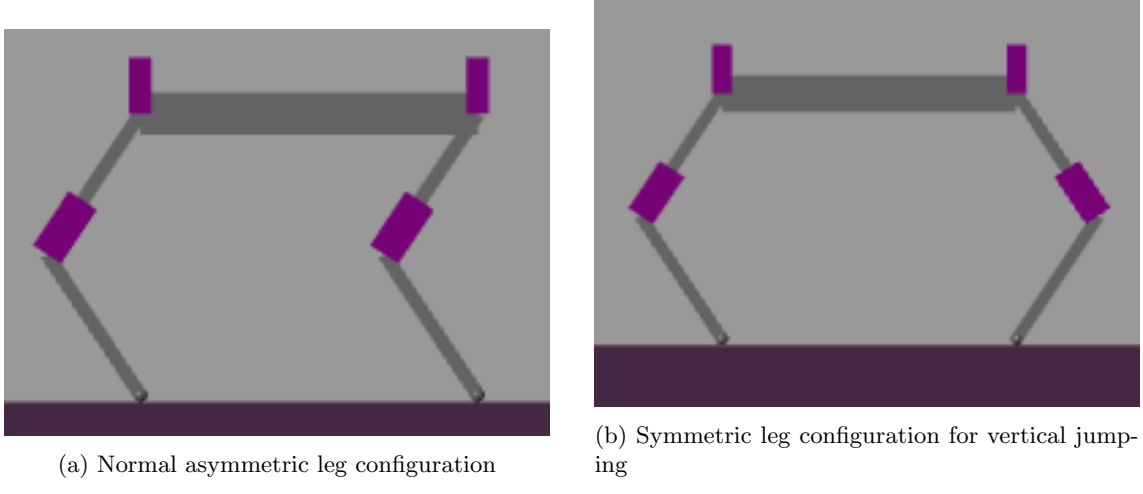


Figure 14: Comparison of normal and symmetric leg configurations

3. $L_1 > L_2$ (longer upper link)

For all cases, we calculate the distance d from hip to paw. For cases $L_1 = L_2$ and $L_1 > L_2$, where paw is placed directly under hip, this distance is vertical from the hip. For case $L_2 > L_1$, where paw is translated horizontally inwards towards the body, this distance is along a vector with angle 0.3 radians inwards towards the body from the vertical. This offset was found to avoid any slipping in most cases, while simultaneously making jumps in the asymmetric leg configuration more realistic.

The distance d should be as small as possible to maximize the knee angle and thus spring load while satisfying the physical constraints of the robot and keeping the paws in contact with the ground. Inverse kinematics then determines the hip and knee angles, selecting the solution where knees bend outward. The distance d is calculated as follows:

- For $L_1 = L_2$: $d = \epsilon$, where ϵ is a small offset ensuring unique inverse kinematics solutions
- For $L_2 > L_1$: $d = L_2 - L_1 + \epsilon$, where ϵ prevents vertical legs and ensures sufficient ground friction
- For $L_1 > L_2$: $d = \sqrt{L_1^2 - L_2^2}$, derived when L_2 is horizontal (maximizing spring load) and forms a right triangle with L_1 and the hip-to-paw vector

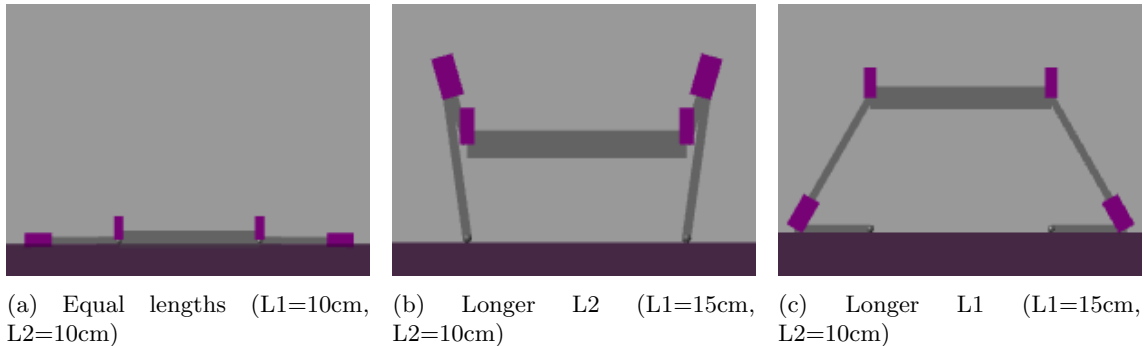


Figure 15: Initial poses for different link length ratios

6.4 Grid Search

The grid search varies two parameters: L2/L1 ratio, and total leg length L1+L2, focusing around $L2/L1 \approx 1$ where preliminary tests indicated generally better performance. Simscape updates the robot mass for each parameter set. Tests were run in both Earth (9.81 m/s^2) and Mars (3.72 m/s^2) gravity, with results in figure ??.

7 Robot Hardware

7.1 Torsional Spring Leg

Figure 16 shows the CAD model for the torsional spring leg design, including both knee and hip extension/flexion motor, as well as the hip adduction/abduction motor.

Figure 17 shows the components that are currently planned to manufacture in inhouse. The axle that will be threaded and screwed directly into the motor shaft, and lead directly into a ball bearing, is emphasized in red. The leg has been designed to make it easily manufacturable in aluminum. Aluminum was chosen as a potential material due to its high strength-to-weight ratio, and the fact that it is easy to machine. Although many easily 3D-printable plastics are generally lighter, they are not as strong as aluminum, in fact aluminum has a much higher weight to yield ratio than 3D printable plastics, and thus, barring complications resulting from manufacture, a leg made in aluminum should be lighter than one made of plastic.

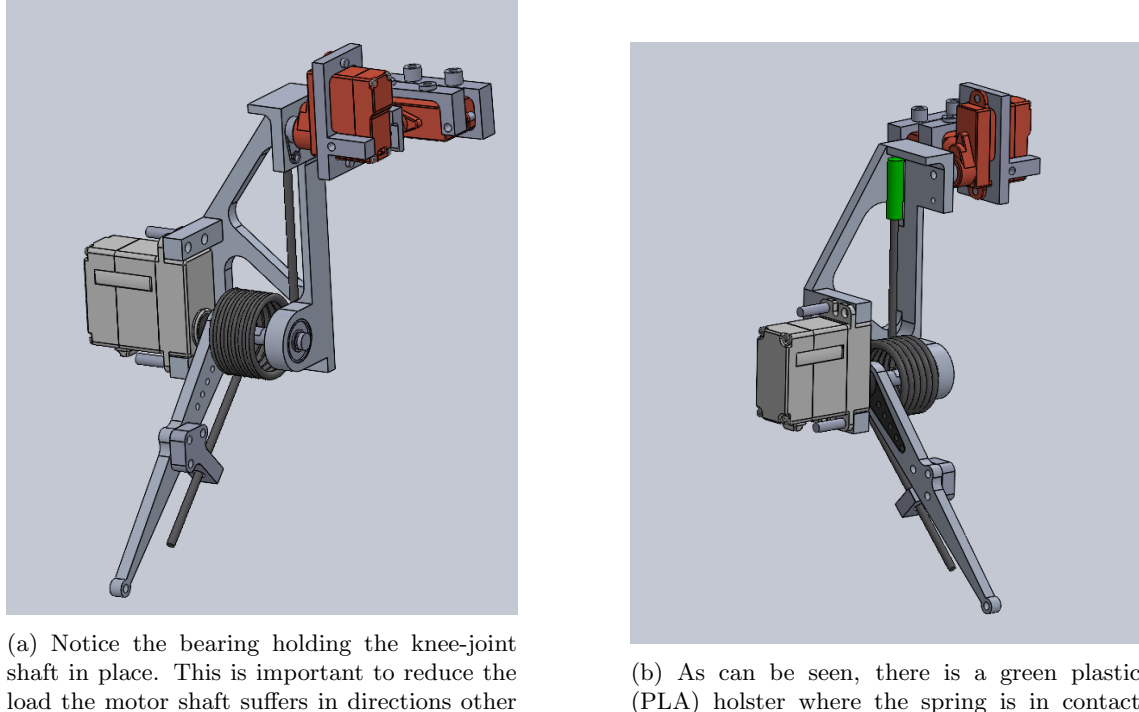


Figure 16: An overview of the leg CAD model with a torsional spring.

A 3D printed version of the leg thigh together with the purchased spring can be seen in figure 18. While the full leg has not been assembled, initial physical load test reveal that the thigh is able to withstand the load of the spring. This could indicate that the leg will be 3D printed rather than made in aluminum.

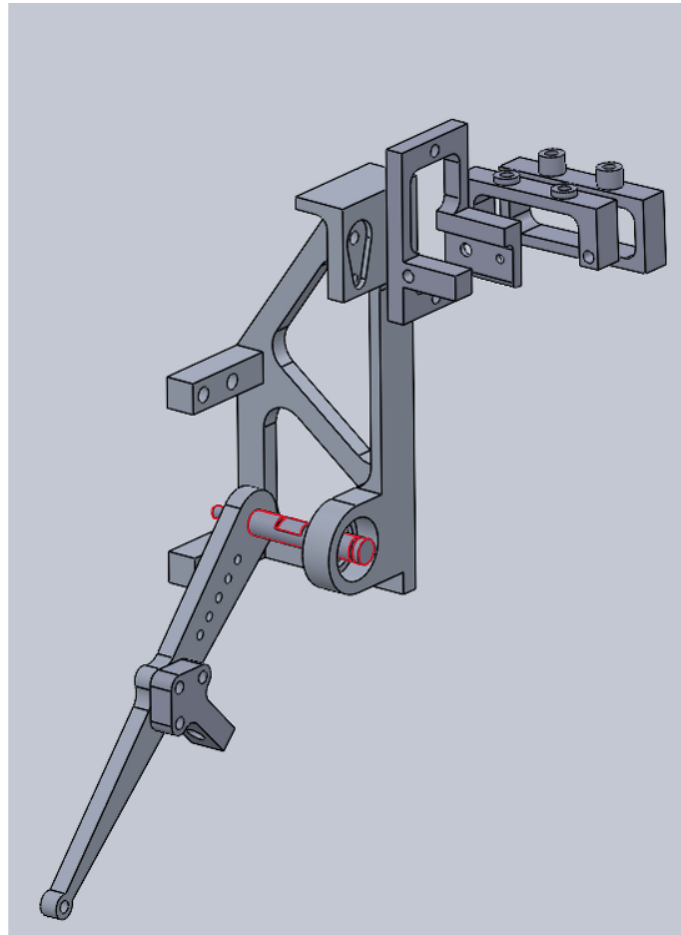


Figure 17: An overview of the CAD model of the leg design, but showing only the components that will be manufactured inhouse. Axel that will be threaded and screwed directly into the motor shaft, and lead directly into a ball bearing, is emphasized in red.



Figure 18: A 3D printed version of the leg thigh with the torsional spring.

7.2 Extension Spring Leg design

The extension spring leg design is shown in figure 19. As can be seen in the figure, the current design is such that the extension spring will collide with the robot shank as the knee angle approaches

± 180 degrees. Despite efforts, no solutions were found for this problem, and this design direction was therefore abandoned. Among the suggested solutions was moving the shank-end attachment point of the spring in the inwards direction, thus allowing the extension spring to lie in parallel next to the shank when the leg is fully coiled. This would however introduce a significant moment arm acting directly on the motor shaft, and this design was therefore abandoned in favor of the torsional spring design.

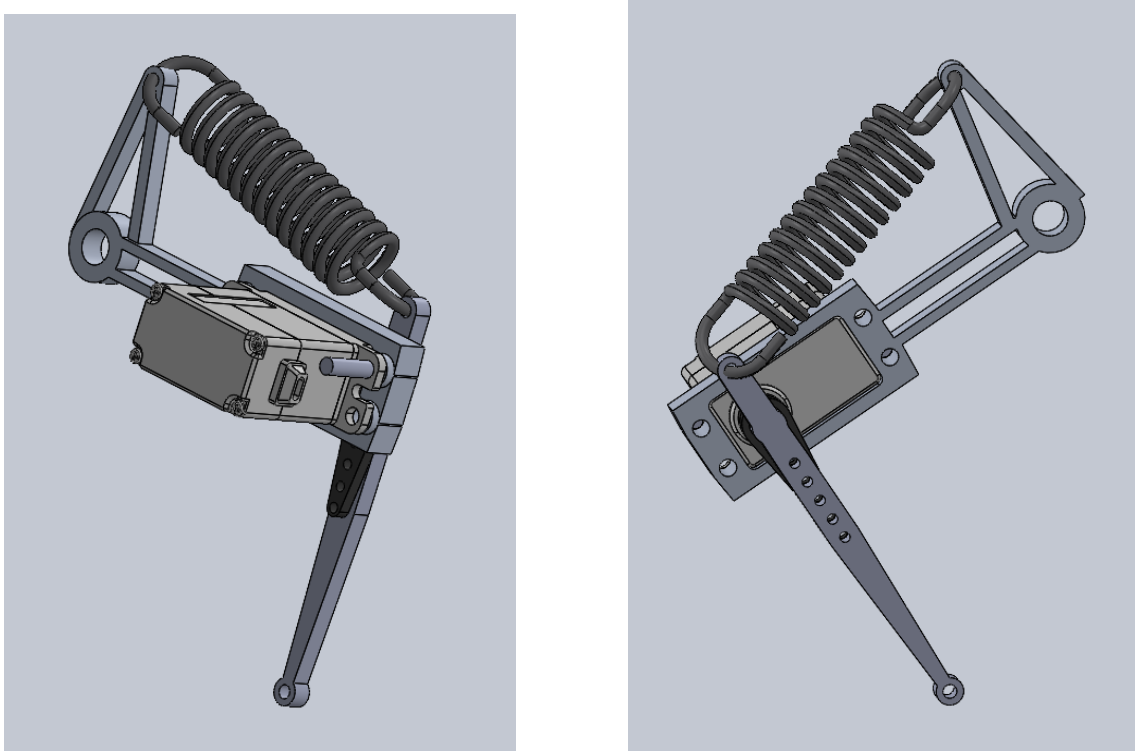


Figure 19: Comparison of extension spring configurations: outside (left) and inside (right) the leg.

7.3 Motor Selection

As discussed in section 4, the choice fell on AGF-RC motors due to their high torque to weight ratio, as well as our inability to find similarly fast motors of similar strength.

Our specific choice of motors can be found in table 5. Info about the specific motors can be found in appendices A to B.

Corresponding Joint	Motor Name
Knee flexion/extension	A20BHM
Hip flexion/extension	A06CLS V2
Hip adduction/abduction	A06CLS V2

Table 5: Selected Motors

The reason these motors in particular were chosen is the fact that no motors were found in a similar weight class that could provide the same torque and speed. For example, if considering AGF-RC motors, the next motor, strength-wise, after the A20BHM motor, is the A35CHM motor, info about which can be found in appendix C. Despite being significantly heavier, the A35CHM motor is only marginally stronger than the A20BHM motor. The reasoning behind the choice of the A06CLS V2 is detailed in 4.5.

8 Results

8.1 Motor Friction Estimation

Pendulum angle θ was sampled with a sampling rate of 60Hz. $\dot{\theta}$ and $\ddot{\theta}$ were derived from θ using numerical differentiation. The viscous damping coefficient b was found to be 0.001 Nm/rad/s for the hip motors (A20 etc) and 0.0001 Nm/rad/s for the knee motors (A14 etc). Figures 20 and 21 show the predicted $\ddot{\theta}$ from the physical models of the pendulum using the estimated viscous damping coefficients, versus the derived $\ddot{\theta}$.

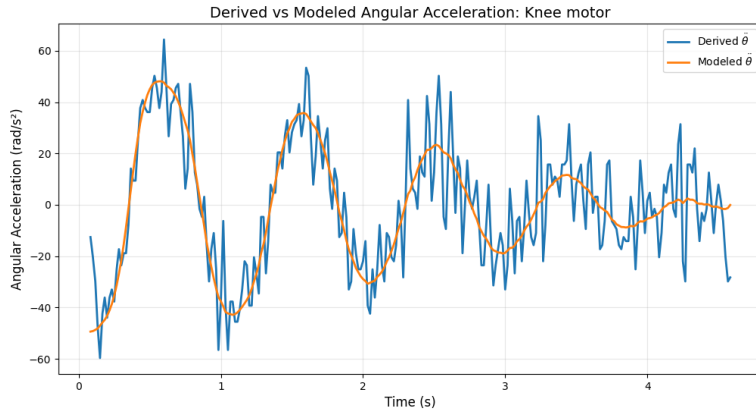


Figure 20: Linear regression fit of the pendulum data for the knee motor. Derived theta dot dot is the double derivative of the pendulum angle.

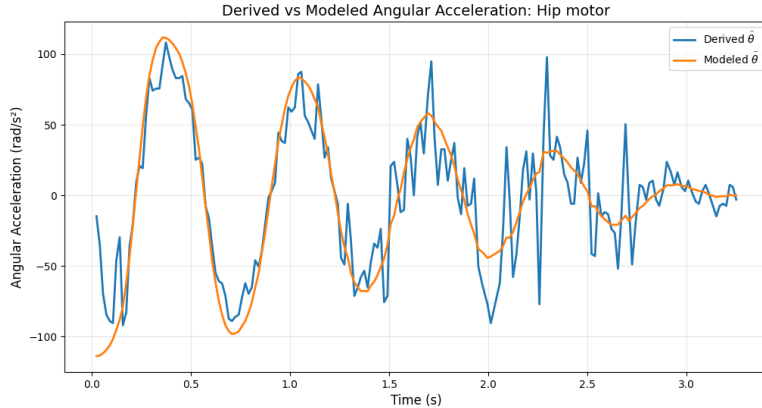


Figure 21: Linear regression fit of the pendulum data for the hip motor.

8.2 Link Length Optimization

The grid search results for both Earth and Mars gravity are shown in figures 22 and 23. The search explored link length ratios from 0.8 to 1.6 and total lengths from 8cm to 36cm, in increments of 0.1 and 0.5 cm respectively.

Best performing jumps are described in table 6.

TODO: Correct optima The optimum total length is 8cm longer under Mars gravity. In both Mars and Earth gravity, the optimal link length ratio is 1.0 across all total lengths, with steep drops in jump height for ratios under 1.0 and less steep drops for ratios over 1.0.

Gravity	Jump Height (cm)	Ratio	Total Length (cm)	L1 (cm)	L2 (cm)
Earth	118.03	1.0	35	12.5	12.5
Mars	31.39	1.0	27	13.5	13.5

Table 6: Best performing link length configurations and their corresponding jump heights for Earth and Mars gravity.

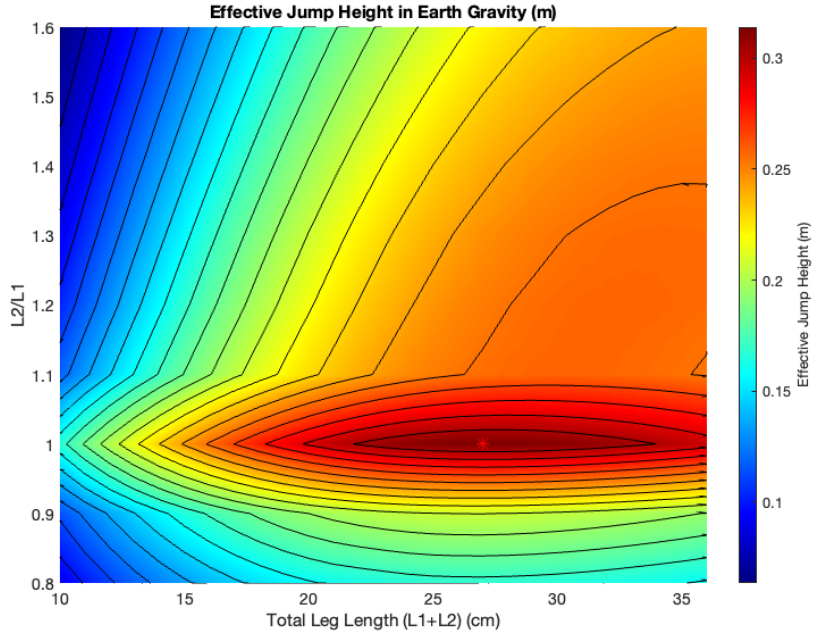


Figure 22: Grid search results showing jump height performance across different link length configurations under Earth gravity.

8.3 Hip Motor Dimensioning Test

As can be seen in figure 24, the hip motors follow the angle reference well, achieving three back and forth swings of 90 degrees over a one second period. The torque output of the motors during this maneuver can be seen in figure 25.

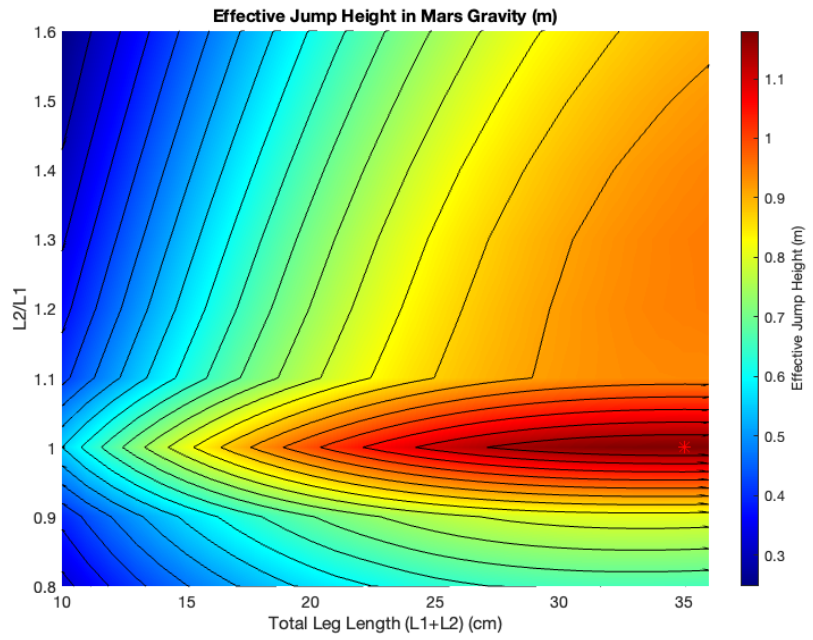


Figure 23: Grid search results showing jump height performance across different link length configurations under Mars gravity.

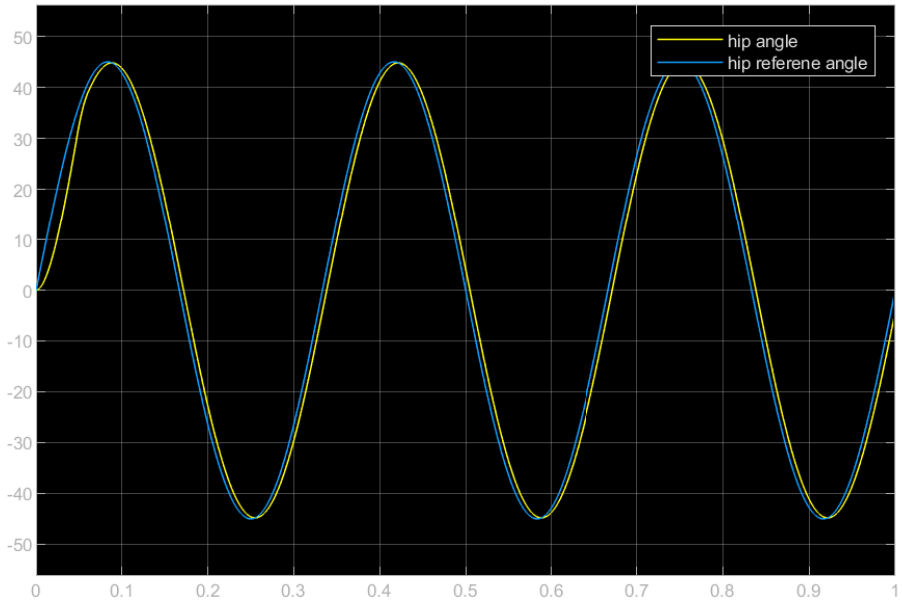


Figure 24: Commanded and actual hip joint angle achieved during the hip motor strength test simulation.

figure 25.

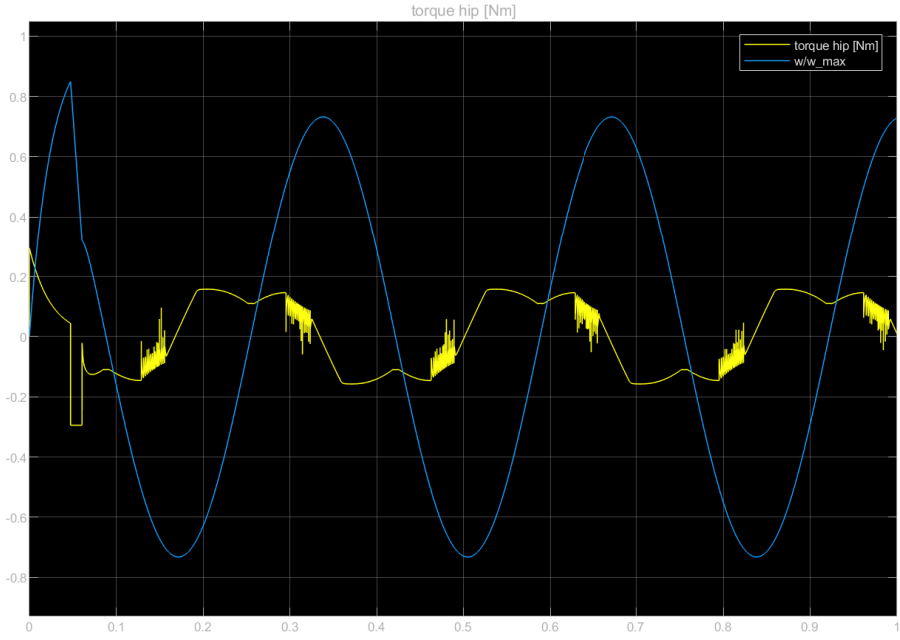


Figure 25: Torque output of the hip motors during the hip motor strength test simulation.

8.4 Motor Only Jumping Results

As described in section 4.2, motor-only simulations were done using the assumed characteristics of the A80BHP-H motor. Because the results were so far from acceptable, only the results of one experiment are presented here, but simulations with shorter leg and body lengths were performed. Figure 26 shows the knee joint actuation torque, knee joint velocity and knee joint angle during takeoff for the A80BHP-H motor. The robot is not able to reach a high enough speed to achieve a good jump, and the peak body center of mass height reached is 70cm, despite a total leg length of 40cm.

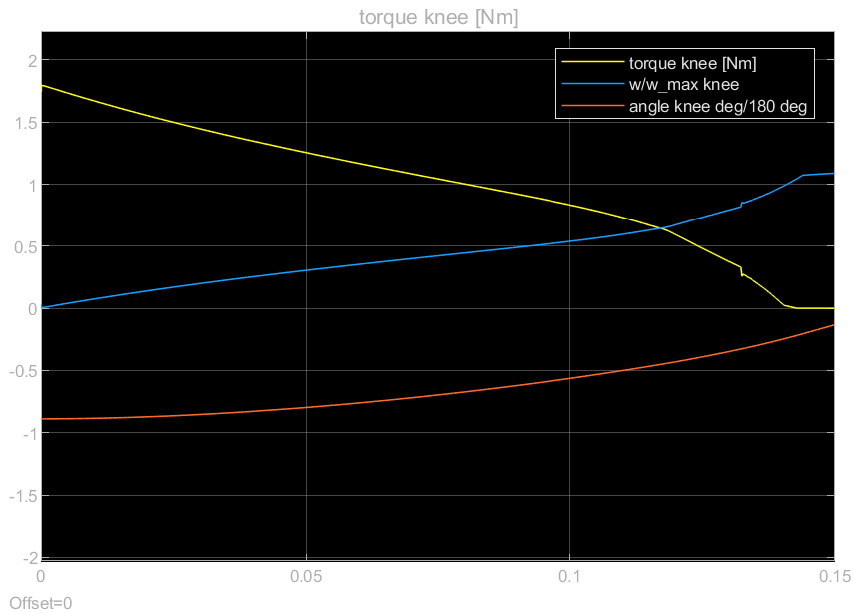


Figure 26: Knee speed until takeoff with A80BHP-H motor.

9 Discussion

9.1 Link Length Optimization Trade-offs

The optimal link lengths found for both Earth and Mars gravity present practical challenges for the mechanical design. The longer lengths would require either elongating the robot body to prevent leg collisions, or translating the hip joints outward. Body elongation would increase overall weight, while outward hip translation raises collision risks during aerial stabilization. Additionally, longer legs increase the inertia that motors must overcome during aerial maneuvers, potentially slowing stabilization response.

Given these constraints, we opted for shorter link lengths that balance jumping performance with mechanical practicality. Future work could incorporate body dimensions into the optimization process. Additionally, activating hip motors during jumps may yield different optima that better align with design constraints.

9.2 Limitations of the Symmetric Jump Model

The symmetric jumping configuration has key limitations in approximating asymmetric jumping performance. For asymmetric legs, achieving a specific jump angle requires careful paw placement relative to the hip joints - a relationship that varies with link lengths. While the symmetric model places paws directly under hips, this same placement in the asymmetric case produces angled rather than vertical jumps.

Experiments show vertical jumps are possible with asymmetric legs by adjusting the hip-to-paw vector angle. However, the symmetric model only partially captures this through a constant angle offset when $L_2 > L_1$, which fails to produce vertical jumps across all link lengths.

This approach introduces systematic biases:

- When $L_1 \neq L_2$: Underestimates jump height since asymmetric vertical jumps require paw positions that angle L_2 and L_1 more horizontally, better converting angular to vertical velocity with less slipping
- When $L_1 = L_2$: Overestimates jump height since achieving vertical jumps requires L_2 to be less horizontal, reducing velocity conversion efficiency

These biases help explain the sharp performance peak at $L_2 = L_1$ in the grid search results (figure ??) for both Earth and Mars gravity.

9.3 Control and Dynamic Challenges

Because the current plan is to turn the knee motors off during jumps, because the torsional springs' power is so much higher than the motors peak power, and it is unknown how the motors will handle that, the current design lacks knee feedback capability during jumps. This could limit the future RL controller's ability to compensate for parameter variations like spring stiffness. This could potentially widen the sim-to-real gap.

When knees bend in the same direction, the shifted center of mass causes uneven leg loading. The back legs bear more weight while the front legs accelerate faster, resulting in backward rotation that complicates aerial stabilization. These challenges could be addressed by using stronger rear springs/motors or by having the hip motors on during the jump with more power provided to the back legs.

9.4 Design Considerations for Landing

The knee spring’s equilibrium position at $\theta_2 = 0$ (straight leg) may complicate landing. To achieve a crouched landing pose, knee motors must work against spring force, increasing response time. Further testing is needed to quantify motor response times for various knee angles.

10 Conclusion

10.1 Future work

The upcoming masters thesis will investigate adding hip motor actuation during jumps to enhance performance and enable feedback control. Then we will use our optimized design to construct the physical robot and create an accurate model in Nvidia Isaac Sim. This model will be used to train reinforcement learning controllers for jumping, aerial stabilization, and landing. Domain randomization techniques will help minimize the sim-to-real gap, and curriculum learning will be explored to make the learning process more tractable. Finally, we will evaluate the trained policies on the physical robot in practical jumping scenarios.

Due to the oversights addressed in section 4.2, the promising A80BHP-H motor was overlooked when selecting motors. This motor not only has almost twice the stall torque of the current knee motor, it also has twice the operating velocity. Future work will include investigating the jumping capabilities of a robot combining this motor with a torsional spring.

11 Conclusion

Bibliography

- [1] Tarek El-Agroudi and Finn Gross Maurer. *In-Flight Attitude Control of a Quadruped in Low-Gravity Environments using Deep Reinforcement Learning*. 2024.
- [2] Andrew Daga et al. *Lunar and Martian Lava Tube Exploration as Part of an Overall Scientific Survey*. White Paper submitted to the Planetary Sciences Decadal Survey 2013-2022. 2022.
- [3] Olav Egeland and Jan Tommy Gravdahl. *Marine Cybernetics*. For ordering, visit <http://www.marinecybernetics.com> or contact info@marinecybernetics.com. Trondheim, Norway: Marine Cybernetics AS, 2002. URL: <http://www.marinecybernetics.com>.
- [4] Ernst Hairer, Christian Lubich and Gerhard Wanner. *Geometric numerical integration: structure-preserving algorithms for ordinary differential equations*. Vol. 31. Springer Science & Business Media, 2006.
- [5] Marco Hutter et al. ‘ANYmal - a Highly Mobile and Dynamic Quadrupedal Robot’. In: *2016 IEEE/RSJ International Conference on Intelligent Robots and Systems (IROS)*. Aug. 2016, pp. 38–44.
- [6] Kevin M. Lynch and Frank C. Park. *MODERN ROBOTICS: MECHANICS, PLANNING, AND CONTROL*. Cambridge University Pres, 2017. ISBN: 978110715630.
- [7] MathWorks. *Getting Started with Simscape*. <https://se.mathworks.com/help/simscape/getting-started-with-simscape.html>. Accessed: 2024-12-15. 2024.
- [8] I. A. Nesnas et al. ‘Axel and Duaxel Rovers for the Sustainable Exploration of Extreme Terrains’. In: *Journal of Field Robotics* 29.4 (2012), pp. 663–685.
- [9] Stephanie Newdick et al. ‘Designing ReachBot: System Design Process with a Case Study of a Martian Lava Tube Mission’. In: *2023 IEEE Aerospace Conference*. IEEE, 2023, pp. 1–9.
- [10] Jørgen Anker Olsen and Kostas Alexis. ‘Design and Experimental Verification of a Jumping Legged Robot for Martian Lava Tube Exploration’. In: *2023 21st International Conference on Advanced Robotics (ICAR)*. 2023, pp. 452–459. DOI: 10.1109/ICAR58858.2023.10406863.
- [11] Jørgen Anker Olsen and Kostas Alexis. *Martian Lava Tube Exploration Using Jumping Legged Robots: A Concept Study*. 2023. arXiv: 2310.14876 [cs.RO]. URL: <https://arxiv.org/abs/2310.14876>.
- [12] Umberto Scarfogliero, Cesare Stefanini and Paolo Dario. ‘Design and Development of the Long-Jumping “Grillo” Mini Robot’. In: *Proceedings 2007 IEEE International Conference on Robotics and Automation*. 2007, pp. 467–472. DOI: 10.1109/ROBOT.2007.363830.
- [13] W.D. Shin, H.V. Phan, M.A. Daley et al. ‘Fast ground-to-air transition with avian-inspired multifunctional legs’. In: *Nature* 636 (2024), pp. 86–91. DOI: 10.1038/s41586-024-08228-9.
- [14] David E Stewart. ‘Rigid-body dynamics with friction and impact’. In: *SIAM review* 42.1 (2000), pp. 3–39.
- [15] Inc. The MathWorks. *MATLAB ODE Suite*. The MathWorks, Inc. Natick, MA, 2024. URL: <https://www.mathworks.com/help/matlab/ref/ode15s.html>.
- [16] Patrick Wensing et al. ‘Proprioceptive Actuator Design in the MIT Cheetah: Impact Mitigation and High-Bandwidth Physical Interaction for Dynamic Legged Robots’. In: *IEEE Transactions on Robotics* PP (Jan. 2017), pp. 1–14. DOI: 10.1109/TRO.2016.2640183.
- [17] Mahboubeh Zarei and Robin Chhabra. ‘Advancements in Autonomous Mobility of Planetary Wheeled Mobile Robots: A Review’. In: *Frontiers in Space Technologies* 3 (2022). ISSN: 2673-5075. DOI: 10.3389/frspt.2022.1080291.

Appendix

A A06CLS V2 Website Information

This information is taken from the website: <https://www.agfrc.com/index.php?id=2666>

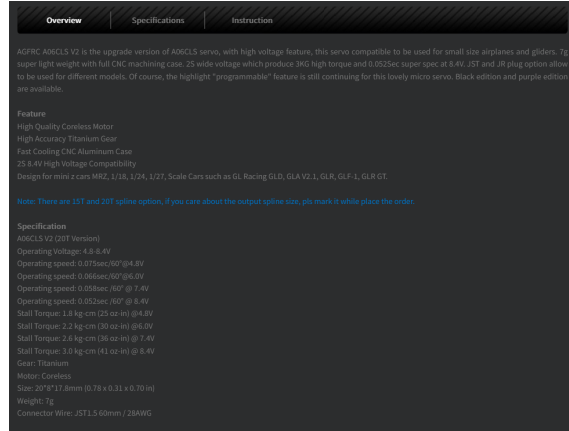
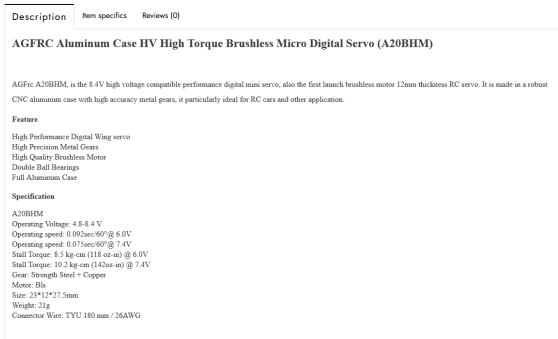


Figure 27: A06CLS V2 Motor Information (Curt)

B A20BHM Website Information

This information is taken from the website: <https://www.agf-rc.com/agfrc-a20bhm-21g-high-speed-0068sec-114kg-programmable.html>



C A35CHM Motor Information

PRODUCT SPECIFICATION A35CHM			
Control System		Pulse width modulation control	
Refresh Rate		333Hz	
Neutral Position		1520uS	
Signal Mode		Digital	
Dead band		2 uSec	
Operating Voltage		4.8V~ 8.4V	
Operating Temperature		-15C~ +70C	
Bearing		Dual Ball Bearing	
Mechanical Limit Angle		220°	
Size		35.5*15*29.2mm	
Net Weight		41g	
Wire		JR 180mm /22AWG	
Operating Travel		180°±10°	
Signal Range		500 to 2500 uSec	
Stall Torque		9.5 kg-cm (132 oz-in) @ 4.8V 10.5 kg-cm (146 oz-in) @ 6.0V 11.5 kg-cm (160 oz-in) @ 7.4V 12.5 kg-cm (174 oz-in) @ 8.4V	
Operating Speed		0.145sec/ 60° @ 4.0V 0.125sec/60° @ 6.0V 0.095sec/60° @ 7.4V 0.085sec/60° @ 8.4V	
Direction		<input checked="" type="checkbox"/> CCW <input type="checkbox"/> CW	
Waterproof Level		<input type="checkbox"/> IP65 <input checked="" type="checkbox"/> IP67	
Angle Sensor		<input checked="" type="checkbox"/> Potentiometer <input type="checkbox"/> Magnet Angle Sensor	
Motor Type		<input type="checkbox"/> Brushless <input checked="" type="checkbox"/> Coreless <input type="checkbox"/> DC	
Motor Drive		<input checked="" type="checkbox"/> FET Drive <input type="checkbox"/> IIC Drive <input type="checkbox"/> Transistor Drive	
Programmable		<input checked="" type="checkbox"/> Yes <input type="checkbox"/> No	
Gear Material		<input type="checkbox"/> Strength Steel <input checked="" type="checkbox"/> Titanium <input type="checkbox"/> Copper <input type="checkbox"/> Plastic	
Horn Gear Spline		<input checked="" type="checkbox"/> 25T+φ5.92mm <input type="checkbox"/> 25T+φ4.94mm <input type="checkbox"/> Other	
Case Material		<input checked="" type="checkbox"/> AL6061T6 <input type="checkbox"/> AL+Plastic <input type="checkbox"/> Plastic	
Bearing Material		<input checked="" type="checkbox"/> Metal <input type="checkbox"/> Plastic	
Horn Accessories		<input type="checkbox"/> AL6061T6 <input checked="" type="checkbox"/> Plastic	
Wire Color		Negative: <input checked="" type="checkbox"/> Black <input type="checkbox"/> Brown Positive: <input type="checkbox"/> Black <input checked="" type="checkbox"/> Red Signal: <input type="checkbox"/> Grey <input checked="" type="checkbox"/> White <input type="checkbox"/> Orange	

Figure 28: A35CHM Motor Information

D A80BHP-H Motor Information

Please note that this brochure gives an operating travel of 90 degrees, this was later confirmed to be false, the actual operating travel is 180 degrees.

SERVO SPECIFICATION			
Operating Voltage	Gear Material	Operating Temperature	Case Material
4.8V ~ 8.4V	Steel	-15C~ +70C	Full Aluminum
Operating Travel	Mechanical Angle	Net Weight	Pulse Width
90°±5°	220°	79g	452 to 1072 uSec
Motor Type	Dead Band	Frequency	Waterproof Level
Brushless	2 uSec	760uS / 666Hz	/
Size	Bearing	Wire	Programmable
40*20*37.5mm	3BB	TYU 300mm / 22AWG	Yes
Operating Speed 0.030Sec / 60° @ 8.4V 0.034Sec / 60° @ 7.4V 0.039Sec / 60° @ 6.0V 0.045Sec / 60° @ 4.8V			
Stall Torque 18.5KG-CM (257 oz-in) @ 8.4V 15.5KG-CM (215 oz-in) @ 7.4V 14.0KG-CM (195 oz-in) @ 6.0V 12.0KG-CM (167 oz-in) @ 4.8V			

Figure 29: A80BHP-H Motor Information